https://doi.org/10.5194/egusphere-2026-4414
Preprint. Discussion started: 11 August 2026

Dual-satellite sea level observations in the ice-covered Southern Ocean, 2002-2024

Isabelle White[1], Oana Dragomir[1], Alessandro. Silvano[1], Alberto Naveira Garabato[1], Anna Hogg[2], Pierre Dutrieux[3], Laura Herraiz-Borreguero[4], Jenny Cocks[2]

[1]FELS, University of Southampton, Southampton, SO17 1BJ, United Kingdom
[2]Institute for Atmospheric and Climate Science (ICAS), University of Leeds, Leeds, LS2 9JT, United Kingdom
[3]British Antarctic Survey (BAS), Polaris House, North Star Avenue, Swindon, SN2 1EU, United Kingdom
[4]Commonwealth, Scientific and Industrial Research Organisation ENVIRONMENT (CSIRO), Castray Esplanade s/n, Hobart, 7004, Tasmania, Australia

Correspondence to: Isabelle F.M. White (i.white@soton.ac.uk)

Abstract

Long-term and spatially continuous data is hard to attain in the remote and harsh environment of the Southern Ocean. Using satellite altimetry, we have been able to measure the subpolar sea surface height (SSH) in the open ocean and sea ice zone since 2002 using Envisat and CrysoSat-2. Here we present a 22-year sea level anomaly (SLA) 1˚ (longitude) by 0.5˚ (latitude) gridded product from 50˚S to the Antarctic coast. This is the longest SLA product to date for the seasonally ice-covered Southern Ocean. We correct for intra- and inter-satellite offsets for the full-time series and overlapping period 01/11/2010 to 01/03/2012, respectively, to level CryoSat-2 data to Envisat. Acquisition modes include synthetic aperture radar interferometry (SARIn), which leads to increased spatial cover and resolution near the coast and decreased product uncertainty. We calculate the product uncertainty using the standard error for offset climatologies, satellite crossover locations and the seasonal variability between four geoids. This results in an uncertainty of 0.78 cm. Validation of our product with the CMEMS reanalysis product, bottom pressure recorders, and other intersatellite products gives average correlations of 0.93, 0.67 and 0.93 (0.81) for the open ocean (sea ice zone), further validating the new product. This product has the potential to improve our ability to identify regional- and large-scale shifts in long-term sea level trends and relate these to climate forcing. It also provides a comprehensive error calculation for a merged Southern Ocean altimetry product.

1 Introduction

Remote monitoring of the Earth surface has been advancing since the launch of the first near-global Landsat1/ERS and Nimbus 5 satellites in 1972 (Bindschadler, 2003; Gallaher and Campbell, 2013). The launch of the SeaSat satellite (Stewart, 1988) (Mccandles, 2003) in 1978 is often considered the start of remote cryosphere observation due to its suite of microwave instruments (Stewart, 1988; Mccandles, 2003), and, in particular, the Synthetic Aperture Radar (SAR). SAR is regarded as one of the most powerful remote sensing methods at our disposal with sub-millimetre accuracy when measuring sea surface height

https://doi.org/10.5194/egusphere-2026-4414
Preprint. Discussion started: 11 August 2026

(Rucci et al., 2012) and a wide range of applications in the Earth's sciences: such as forest floor spectral properties (Mercier et al., 2025), polynya characterisation (Inserra et al., 2024), sea ice motion measurements (Leberl et al., 1983) and sea surface current retrieval (Pan et al., 2025).

However, due to its limited coverage north of 72N and south of 72S, the poles remained under sampled. The equivalent 'start date' for the polar monitoring record is associated with the 1991 launch of the ALT and SAR based European Remote Sensing (ERS-1) program, which covered up to 82˚N-82˚S and provided a valuable tool for open-ocean observations (Teleti and Luis, 2013; Zhang et al., 2022). More recently, the 2002 and 2010 launch of Envisat and CryoSat-2 have furthered our ability to monitor these environments with their 88˚N-88˚S latitudinal extent and ~1 km and 300 m resolution, respectively (Benveniste et al., 2004; Esa, 2019).

In Antarctica, the high concentration of sea ice increases the error associated with altimetric observations over the Southern Ocean (Armitage et al., 2016; Andersen et al., 2019; Rye et al., 2014), despite advancements in monitoring and processing technology. Addressing observational challenges directly is important because about 40% of the anthropogenic carbon and 80% of its heat absorbed by the ocean occurs in the Southern Ocean so systematic changes in the Southern Ocean are of global importance. For example, intensification of the upper (Gülk et al., 2026) or weakening/meridional shifting of the lower (Wyatt et al., 2026; Van Wijk and Rintoul, 2014) limb of the Southern Ocean Overturning Circulation impacts heat and nutrient redistribution and subsequently important ecosystems (Thresher et al., 2026). By capturing ocean currents such as gyres, coastal currents and the Antarctic Circumpolar Current (ACC) using SSH, we can study heat redistribution pathways or changes in freshwater content (Cocks et al., 2025) and better understand relationships between the atmosphere, the ocean and the Antarctic Ice Sheet.

A fundamental shift for decreasing uncertainty and increasing data coverage occurred in 2004 when Peacock and Laxon (2004) disentangled sea surface height (SSH) in ice covered regions in the Arctic using the difference in return waveforms for open ocean vs sea-ice leads between May 1995 and June 1999 for the ERS satellite. Since 2004, multiple studies have used this method to improve the accuracy of or extend along-track SSH data sets in the Arctic. For example, Armitage et al. (2016) used Gravity Recovery and Climate Experiment (GRACE) and radar altimetry to calculate SSH variability due to steric height, (Prandi et al., 2012) used a multi-mission approach to produce a mean sea level (MSL) from 1993-2009, and Veillard et al. (2024) utilised advancements in remote sensing capabilities and resolution to produce a high resolution (~1 km) product between 2011-2021.

Although this method was established in 2004, it was more than a decade later when it was first applied to Antarctica by Armitage et al. (2018) and (Dotto et al., 2018) resulting in a 5-year dataset between 2011-2016 using the CryoSat-2 satellite.

https://doi.org/10.5194/egusphere-2026-4414
Preprint. Discussion started: 11 August 2026

Other studies have since also used this method to extend data coverage and expand current understanding of key knowledge gaps.

For example, the impact of Antarctic sea ice seasonality on steric height (Cocks et al., 2025), variability in the Ross Gyre driven by seasonal and semi-annual forcing (Dotto et al., 2018), and the processes linking sea ice coverage to eddy density and amplitude (Auger et al., 2023). Additionally, Auger et al. (2022) and Mosneron Dupin et al. (2025) developed multi-mission satellite products combining CryoSat-2, Sentinel-3A and SARAL/AltiKa over 2013-2019 and 2003-2021 respectively, with the latter also incorporating Envisat. These datasets have both improved our ability to monitor long-term trends in the Southern Ocean.

Understanding the impact of climate forcing on Southern Ocean systems, such as gyre characteristics or response to climate indices through processes like tropical teleconnections, requires continuous SSH records long enough to resolve, and therefore interpret, inter-annual signals. To date, these relationships have been challenging to study due to the lack of long-term observational SSH data, which can restrict pan-Antarctic impact assessment to studies using limited observational and potentially biased model-based investigations (Li et al., 2021; Doddridge et al., 2025). The multi-mission dataset presented here addresses this data gap directly by providing over 20 years of continuous SSH measurements with quantified uncertainties, making it well placed for long-term oceanographic analysis. For example, this product covers the sea-ice covered region of the Southern Ocean both before and after the recent decline in Antarctic sea ice since 2016 and therefore supports research into the role of ocean processes on sea ice extent or concentration.

We combine Envisat and CryoSat-2 SSH data using the methodology from Peacock and Laxon (2004), Armitage et al. (2016) and (Dragomir, 2024) to correct for ocean-lead offset in sea ice regions. We then calculate the offset between each CryoSat-2 acquisition mode: Low Resolution Mode (LRM), Synthetic Aperture Radar (SAR), and Interferometric SAR (SARIn). Once these offsets have been corrected for each satellite, we use the mission overlap period between 11/2010-03/2012 to calculate the inter-satellite offset before levelling CryoSat-2 to Envisat. We then calculate the root mean squared SLA difference for the overlap period and quantify SLA uncertainty using crossover locations (Armitage et al., 2016; Giles et al., 2012; Peacock and Laxon, 2004). The inclusion of SARIn and error calculation expands on previous work and, in addition to this, the processing pipeline has been designed to support the integration of new data, so long-term analysis can continue.

2 Data

The dataset presented here expands on previous work in terms of spatial and temporal coverage, error characterisation, and validation against other SSH datasets. The data used for this product can be categorised as those used for analysis and those used for validation and are detailed in Sect. 2.1 and Sect. 2.2 respectively.

https://doi.org/10.5194/egusphere-2026-4414
Preprint. Discussion started: 11 August 2026

2.1 Altimetry Data

We use data from the radar altimeter, RA2, on Envisat and the Sar Interferometric Radar Altimeter (SIRAL) on CryoSat-2. Details on each satellite acquisition is outlined in Table. For both satellites, we use data collected by the European Space Agency (ESA) and processed by the Centre for Polar Observation and Modelling (CPOM) and University College London (UCL).

Table 1: Satellite missions used in the product, adapted from Mosneron Dupin et al. (2025)

Satellite	Operational Dates	Mode over open ocean	Mode over sea-ice	Retracking for leads	Resolution (km)	Sampling Rate (Hz)	Inclination (degrees)	Latitudinal Extent (degrees)	Cycle Duration (days)
Envisat	01-03-2002 to 08-05-2012	LRM	LRM	Adaptive	~1	18	99 °	88°N-88°S	35
CryoSat-2	08-05-2010 to present	LRM	SARM/SARIn	TFMRA	0.17	20	92 °	88°N-88°S	369 (30-day pseudo cycle)

2.1.1 Envisat

Envisat was a sun synchronous satellite, with an orbit altitude of 800 km and a repeat cycle of 35 days. Mapping between ± 82° latitude at an along-track sampling resolution of 372 m, Envisat continued the delivery of high-latitude data previously provided by ERS-1 and ERS-2 (Tilling et al., 2019; Teleti and Luis, 2013).

The RA-2 used on Envisat is a standard Low Resolution Mode (LRM) altimeter with a default Ku-band operating frequency of 13.6 GHz and a secondary S-band frequency of 3.2 GHz. The two operating frequencies enable the correction on the S-band for the ionospheric delay (Schmid et al., 1966) and fine-scale structures, like crevasses (Lacroix et al., 2007). Additionally, RA-2 uses Model-Free Tracker (MFT) software, which automatically changes acquisition resolution depending on the echo received (Roca et al., 2009; Resti et al., 1999). For our product, this relates to a surface change from open ocean to sea ice to land.

https://doi.org/10.5194/egusphere-2026-4414
Preprint. Discussion started: 11 August 2026

2.1.2 CryoSat-2

CryoSat-2 is a non-sun-synchronous satellite where measurements over the same location occur at different times of day, an altitude of 730 km and a quasi-repeat cycle of 369 days. It also has a near complete monitoring range of latitudes between ± 88˚(Esa, 2019).

The SAR/Interferometric Radar Altimeter-2 (SIRAL) instrument design improves the transition from the sea ice zone surrounding Antarctica to the Antarctic continent. The SIRAL instrument has two antennas. The first antenna is a conventional pulse-limited radar and the second is a synthetic aperture capable of interferometric (SARIn) processing. The use of a dual antenna system, especially when one is a synthetic aperture, results in the 'appearance' of a longer antenna, therefore increasing the spatial resolution of CryoSat-2. This makes it possible to solve the ambiguity of reflector source direction over rough terrain or slopes which is critical in the transition from the sea ice zone surrounding Antarctic to ice shelves (Chuter and Bamber, 2015; Jonathan and Charles R, 1994). SIRAL has three operating modes: low resolution (LRM) for open ocean, SAR altimetry (Downes et al., 2011) for flat sea-ice areas, and SAR Interferometric (SARIn) for steeply sloping margins (Esa, 2019; Wang et al., 2015). The LRM is like that on ENVISAT (Benveniste et al., 2004) with SARM and SARIn improving along-track footprint to 170 m (Aublanc et al., 2021; Gourmelen et al., 2018).

2.2 Auxiliary Data

2.2.1. Multi-mission Satellite Data

We use the DUACS multi-mission processed Absolute Dynamic Topography (ADT) data from Global Ocean Gridded L 4 Sea Surface Heights and Derived Variables Reprocessed 1993 Ongoing. E.U. Copernicus Marine Service Information (Cmems). Marine Data Store (MDS). DOI: https://doi.org/10.48670/moi-00148 (Accessed on 09 Dec 2025). This is the the sea surface height above the geoid and is an Optimal Interpolation of along-track measurements. We then use linear interpolation to re-grid this data set to 1˚ longitude by 0.5˚ latitude to enable comparison to our dataset.

We also compare our product to the multi-mission sea level anomalies product developed by Mosneron Dupin et al. (2025) which is available from: https://doi.org/10.5281/zenodo.17467408. This product combines Envisat, CryoSat-2, SARAL/Altika, and Sentinel-3A observations between 2003-2021. Several features differentiate our approach to Mosneron Dupin et al. (2025). Aside from the 3-year increase in temporal coverage that our dataset provides, we also include the SARIn mode on CS2 which decreases coastal uncertainty. Both processing pipelines use the reflected waveforms to identify open ocean and lead reflectors and correct for offset/bias. However, Mosneron Dupin et al. (2025) calculated the offset between the SARM SSH of CryoSat-2 and Sentinel-3A and applied this correction to Envisat and Saral, whereas we use the Envisat-CryoSat-2 offset because the open ocean LRM acquisition is the area of largest overlap between the two satellites. Another

https://doi.org/10.5194/egusphere-2026-4414
Preprint. Discussion started: 11 August 2026

difference is their use of CryoSat-2 as the baseline, while we use Envisat when correcting for inter-mission offset. For both offset calculations, a 75 km x 75 km x 10-day bins are used rather than our 1˚ longitude by 0.5˚ latitude monthly bin which accounts for the lower spatial resolution of Envisat and quasi-repeat cycle for CryoSat-2.

These processing differences add to the value inter-product validation as they highlight product independence. Here we calculate the residual offset between the products and the spatial distribution of the error.

2.2.2. Bottom Pressure Data

We use daily Bottom Pressure Recorders (BPR) measurements to quantify the relationship between the SSH in our product and sub-surface pressure (SSP). We use BPRs MYRTLE B, MYRTLE C, Drake Passage South (DPS), and Drake Passage South Deep (DPSD) from the Permanent Service for Mean Sea Level (PSMSL) by the National Oceanography Centre and ANT17.1 from PANGAEA (https://psmsl.org/data/bottom_pressure/table.php, https://doi.pangaea.de/10.1594/PANGAEA.912236, respectively) because these BPRs overlap our time period. Also, they are both North and South of the barotropic potential vorticity (*f/H*) contours, which are the bounds for the barotropic transport mechanism termed the 'Southern Mode' (Hughes et al., 1999) where sea level and bottom pressure vary coherently around Antarctica. These geostrophic contours roughly align with the 1000m isobath (Marshall, 1995; Moorman, 2019) so are used here for the boundary between processes on and off the Antarctic continental slope. By testing locations either side of the Southern Mode bounding contour, we can explore the SSH-SSP relationship within our dataset. Additionally, Hughes et al. (2003) show that the coherence between sea surface pressure (SSP) and bottom pressure (BP) is strongly influenced by bottom topography and, therefore, the relationship is inconsistent far from the coast. Vinogradova et al. (2007) further investigate this relationship and find BP is equivalent to sea level for ~100-day periods at latitudes >60˚S and shallow, < 200m, depths. This is because there is a delay before the adjustment from barotropic (redistribution of water column mass) to baroclinic (internal density variation) changes in SSH.

Near-bottom pressure mooring (BPM) timeseries data from the OCEAN:ICE dataset (Zhou et al. (2025)) is another means to explore our product's ability to capture barotropic adjustment. The OCEAN:ICE dataset is available from: https://doi.org/10.17882/109453 and is a circumpolar compilation of moored bottom pressure timeseries less than 50 m off the seabed south of 60˚S. It is complimentary to the daily BPRs because it has wider spatial and temporal coverage so can be used to highlight systematic/regional differences in correlation.

2.2.3. Southern Annular Mode

The Southern Annular Mode (SAM) is a dominant mode of atmospheric variability in the Southern Hemisphere and is calculated as the difference in zonal sea level pressure between 40˚S and 65˚S (Gong and Wang, 1999). A positive SAM index, where pressure indicates an increase in pressure at 40˚S and reflects strengthening of the circumpolar westerlies around Antarctica (Marshall, 2003). We use the monthly SAM index from https://legacy.bas.ac.uk/met/gjma/sam.html to compare index strength and sea level anomaly from the dataset.

https://doi.org/10.5194/egusphere-2026-4414
Preprint. Discussion started: 11 August 2026

3. Methods

Satellite altimetry uses the time between transmission and receival of a nadir radio wave to estimate the range to the Earth's surface using knowledge of the satellite's orbit for each acquisition mode (Fig. 1). In addition to the distance to the Earth's surface or the ocean's topography, by examining the roughness, shape and power of the reflected wave, known as the waveform, the surface type (open ocean or sea ice), can be estimated (Chelton et al., 2001). In the Southern Ocean retracking is particularly important in sea-ice covered regions where SSH is typically over-estimated (Wernecke and Kaleschke, 2015). These regions have ice floes and leads which are individual pieces of ice in the ocean and the open water fractures between them. Due to the sheltering effect of the ice, lead-based reflected waves are specular, so have a high pulse peakiness and power relative to the surrounding ice (Peacock and Laxon, 2004). This differentiation enables SSH calculation despite sea ice cover.

We use data from the Envisat and Cryosat-2 missions and a combination processing techniques from Armitage et al. (2016), Dotto et al. (2018), A Hooley (2018) and (Dragomir, 2024) to create a dataset which is consistent for both the open-ocean and sea-ice zone. The sections below outline our processing pipeline which culminate as over 20 years of SLA data.

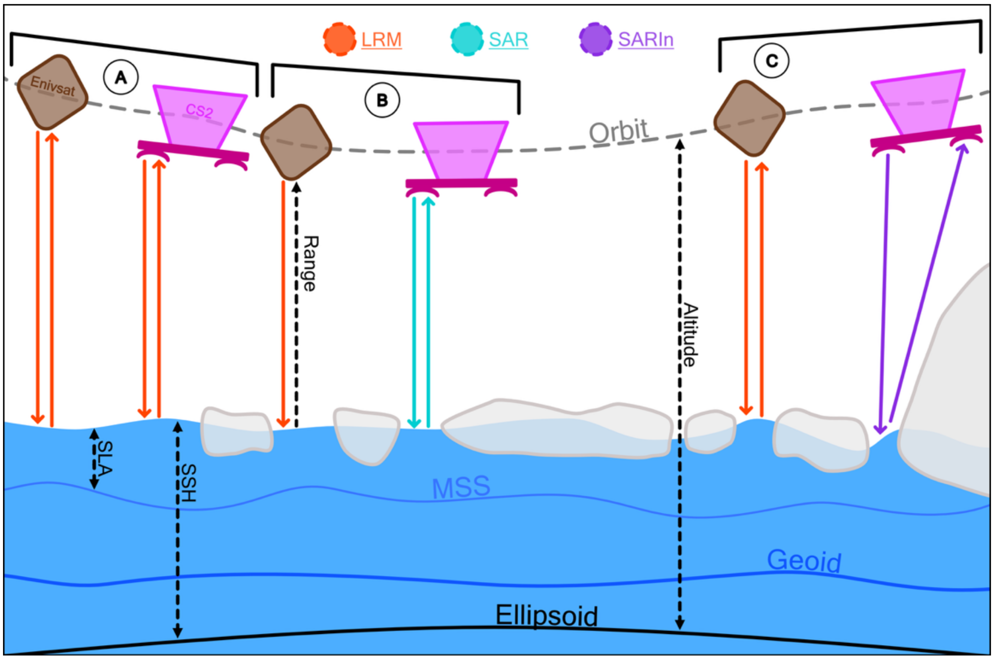

Figure 1: Radar altimetry modes for Envisat and CryoSat-2 (CS2) across open ocean (A), sea ice (B), and costal/steep-slope regions (C). Envisat only operates using LRM, whereas CryoSat-2 switches to SAR over sea ice, increasing sampling from ~20 Hz to ~20,000 Hz. In costal/steep regions with very narrow lead openings, CryoSat-2 uses SARIn and the associated dual antennae to calculate phase differences for off-nadir reflectors and achieve ~300 m resolution.

https://doi.org/10.5194/egusphere-2026-4414
Preprint. Discussion started: 11 August 2026

3.1. Along-Track Processing

The along-track data from CPOM/UCL have been corrected for a range of geophysical parameters, accounting for dry and wet tropospheric, ionospheric, inverse barometric, dynamic atmospheric, ocean tide, ocean loading tide, long period ocean tide, geocentric pole tide and solid earth tide effects (Resti et al., 1999). The SSH has been calculated using the methods from Peacock and Laxon (2004). Slope correction is also applied for LRM and SARIn CryoSat-2 data using a slope model and interferometric phase respectively (Esa, 2019). This data is presented as Level 2 Baseline C monthly text files (Bouffard et al., 2018) with sea surface height (SSH) referenced to the WSG84 ellipsoid.

CryoSat-2 data are initially separate LRM, SAR, and SARIn files, with which we calculate the distance-to-land. We then filter the monthly files removing data that is flagged as not valid, has a confidence in sea ice type lower than 'good' or has a sea surface height anomaly >|3m|, as this is too large for the open ocean. These filtered files are combined to produce monthly mode files to enable comparison and compatibility with Envisat, the full list of variable names is in Table A1. We also use distance-to-land to remove points less than 10 km from the coast as well as to remove files which have more than 1% of points on land. The final stage of the along-track data pre-processing is done by plotting the number of points per bin, where a bin is 1˚ longitude by 0.5˚ latitude. We use this to identify low coverage months and remove them from the dataset.

3.2. Ocean-Lead Offset

To identify ocean and leads within our data, we use the 'SurfaceType' flag to separate returns. We calculate the sea surface height anomaly (SSHA) from the SSH and mean sea surface (MSS) using:

$$SSHA = SSH - MSS, \tag{1}$$

where MSS is calculated using both a one-year (28-01-2011 to 31-01-2012) period to average high frequency SSH components and low frequency component from 03-2011 (Naveira Garabato et al., 2019). We do this for ocean and lead reflectors separately before gridding the data onto a regular longitude-latitude grid, masking land-based data points and recording the number of points in each bin per month. We then calculate the area-weighted average

$$\bar{x} = \Sigma w_i x_i \, , \tag{2}$$

where

$$w_i = \frac{Binned\ Area}{Total\ Valid\ Area}, \tag{3}$$

https://doi.org/10.5194/egusphere-2026-4414
Preprint. Discussion started: 11 August 2026

for bins containing more than 30 data points of the offset between ocean and lead SSHAs to produce an offset climatology for each satellite as shown in Figure 2. We calculate the average using both the mean and median, aiming to select the best statistics based on the total overlap root mean square difference using a range of offsets. This is detailed in Sect. 3.4.

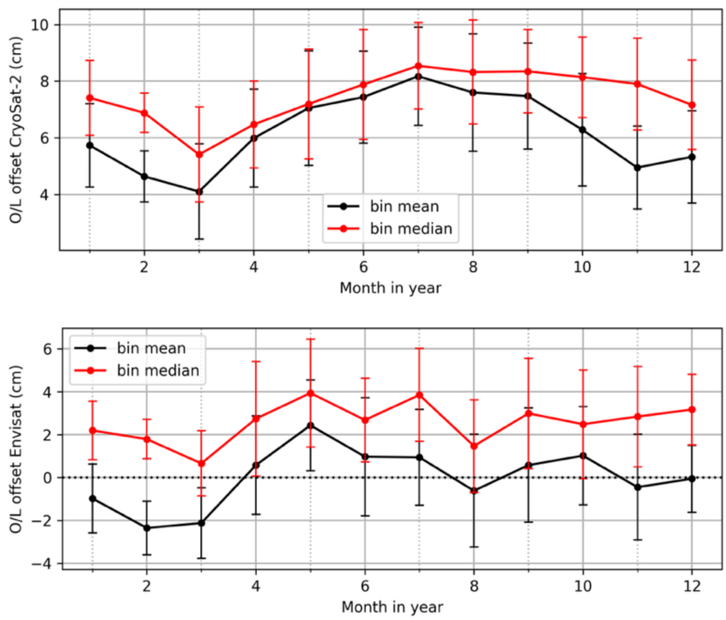

Figure 2 Ocean-lead (O/L) mean and median offset climatology for: Top: Envisat and, Bottom: CryoSat-2.

3.3. CryoSat-2 Mode Offset

As Envisat only has one acquisition mode, calculating the ocean-lead offset is the biggest part of producing a continuous data set. However, for CryoSat-2, we must also correct for the offset between LRM, SAR, and SARIn modes. We follow the same logic as in Sect. 3.2.; using the ocean-lead offset climatology to level recorded SSH before computing SSHA and binning depending on the retracker. We then compute mode offsets to produce a new mode offset file containing:

$$LRM - SAR = binned(LRM) - binned(SAR), \tag{4}$$

and

$$SAR - SARIn = binned(SAR) - binned(SARIn), \tag{5}$$

we do not directly calculate the offset between LRM and SARIN due to the lack of spatial overlap (Fig. 3) which would increase uncertainty associated with this correction. Instead, we chain the offsets to calculate

$$LRM - SARIn = (LRM - SAR) + (SAR - SARIn), \tag{6}$$

https://doi.org/10.5194/egusphere-2026-4414
Preprint. Discussion started: 11 August 2026

From these offsets, we again calculate the area-weighted average of the offsets using mean and median statistics to produce an offset climatology with the associated standard deviation for each month (Fig. 4).

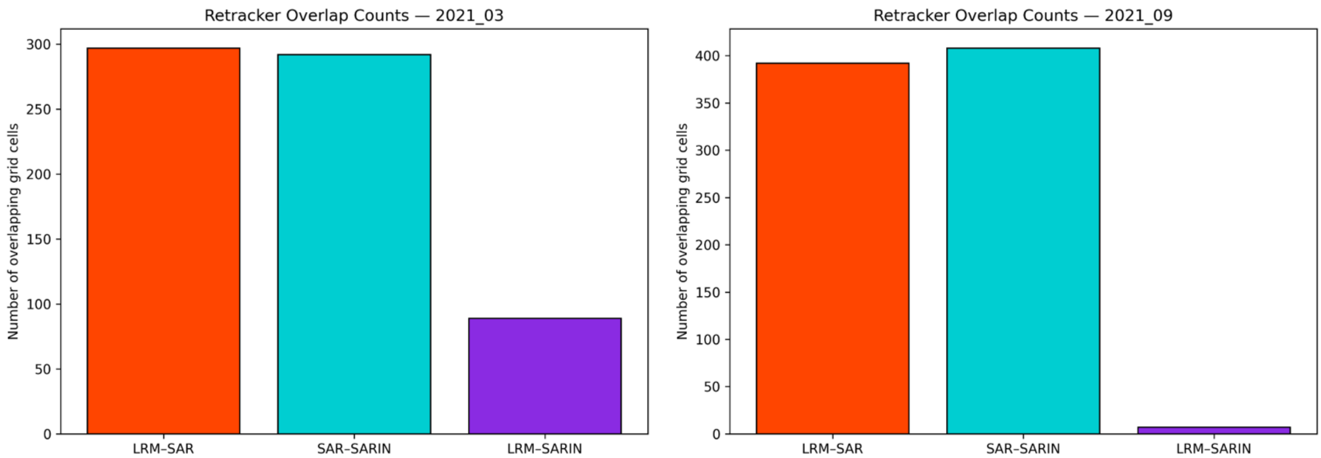

Figure 3: Example charts of the number of spatially overlapping grid cells for each pair of retracker modes in CrysoSat-2 for both Austral Summer (left) and Winter (right). LRM and SARIN have little to no spatial overlap hence we compare LRM and SAR, and SAR and SARIn.

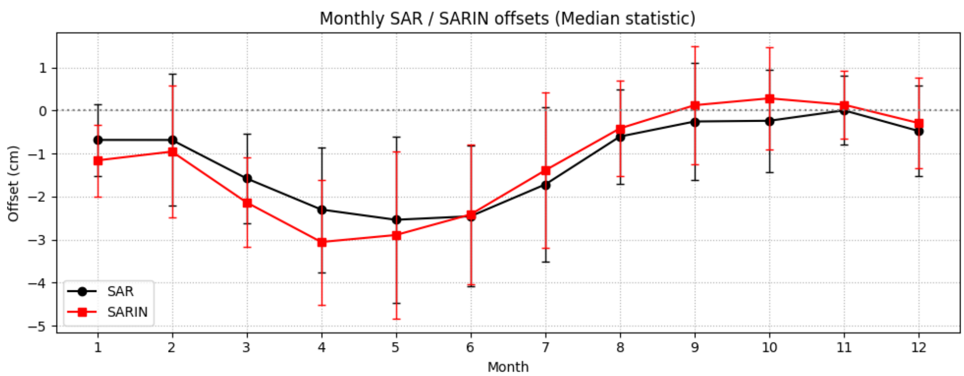

Figure 4: LRM-SAR and LRM-SARIN mode offset climatology for median for CryoSat-2 with error bars representing temporal standard deviation within each month.

3.4. Intersatellite Offset

Before applying the offset climatology for each offset, shown in Figure 2 and Figure 4, we interpolate each geoid onto the raw along-track longitude and latitude values to calculate the Dynamic Ocean Topography (DOT) using

$$DOT = SSH - Geoid, \tag{7}$$

https://doi.org/10.5194/egusphere-2026-4414
Preprint. Discussion started: 11 August 2026

and SLA relative to the Envisat MSS during the overlapping period 01/11/2010 to 01/03/2012.

$$SLA_{ENV} = DOT_{ENV} - MDT_{ENV}, \tag{8}$$

$$SLA_{CS2} = DOT_{CS2} - MDT_{ENV}, \tag{9}$$

for four independent geoids, Table 2. This approach allows us to compare our final product's uncertainties and, therefore select which geoid is the most precise. We test both satellite (only satellite data) and combined (complimentary satellite, terrestrial and airborne data) geoids.

Table 2 Geoid summary table (Liang et al., 2020; Förste, 2016; Fecher, 2016; Öhlinger, 2025). Accessed from: https://icgem.gfz.de/home.

Geoid	Geoid Type	Degree (number of spherical harmonics)	Spatial Resolution (km)	Year	RMS (cm)
EGM2008	Combined	2190	~ 10	2008	0.052
EIGEN6S4V2	Satellite-only	300	~ 10	2014	0.064
GOCO05C	Combined	720	~ 28	2016	0.053
GOCO2025S	Satellite-only	300	~ 70	2025	0.073

Once the SLA is calculated for both satellites, we calculate the intersatellite offset as

$$Intersatellite\ Offset = SLA_{ENV} - SLA_{CS2}, \tag{10}$$

for each grid cell at each overlapping month before calculating a time mean of these and calculating an area-weighted average of the entire product area where the offset is positive, see Figure 5. The negative regions in Figure 5 are excluded from this offset because they correspond to shallow bathymetry areas, like Crozet Island and the Kerguelen Plateau, which are likely to have strong semi-/di-urnal tide SLA signals that are poorly resolved by our monthly product (Maraldi et al., 2011; Lelièvre et al., 2025). We correct CryoSat-2 with the inter-satellite offset before calculating residual variability, again masking the areas identified as impacted by tides. We use the area-weighted RMS for each geoid as well as multiple combinations of mean/median climatology and offset averages to assess the best method for the processing pipeline. We find the EGM2008 geoid to have the lowest RMS at 0.052 cm and the GOCO2025S the highest at 0.073 cm (Table 2). As the difference between geoids is small, we now only present the EGM2008 dataset.

https://doi.org/10.5194/egusphere-2026-4414
Preprint. Discussion started: 11 August 2026

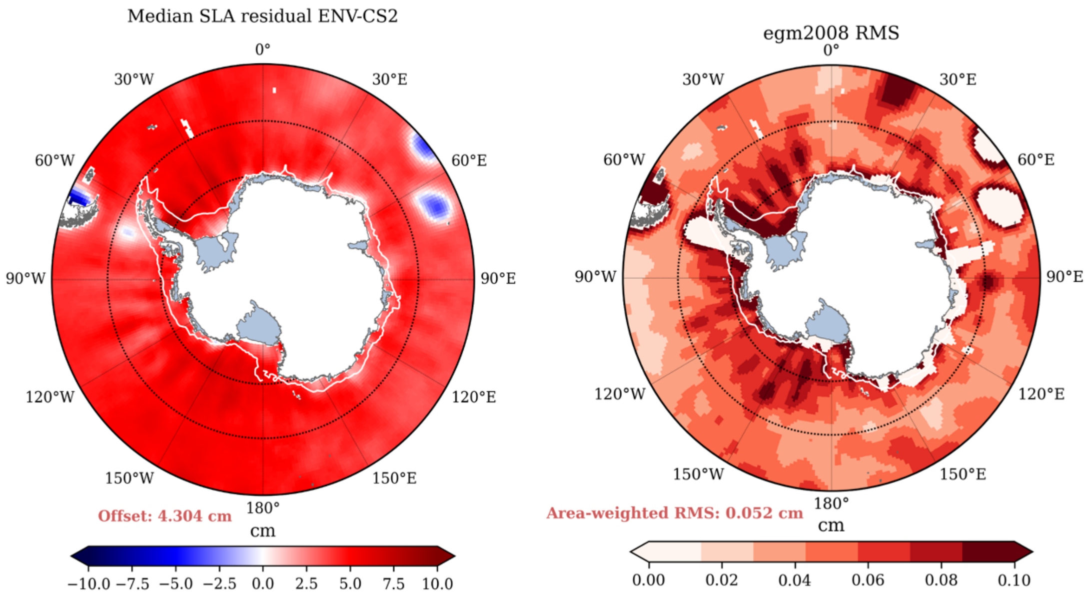

Figure 5: Left: median SLA inter-satellite residual referenced to the Envisat MDT for the overlapping period 01-07-2010 to 01-03-2012. This has a 4.30 cm median offset. Right: root mean square for each grid cell after the offset has been applied to CryoSat-2. Area-weighted average is 0.052 cm.

3.5 Satellite Merging

For the final stage of our pipeline, we bring CryoSat-2 level to Envisat, using the offset calculated in Sect. 3.4., for all files outside of the overlapping period. During the overlapping period we take the mean DOT per grid. We calculate surface geostrophic velocity relative to the DOT using

$$u_g = -\frac{g}{f}\frac{\delta DOT}{\delta y}, \tag{11}$$

$$v_g = \frac{g}{f}\frac{\delta DOT}{\delta x}, \tag{12}$$

where g is gravity, f is the Coriolis parameter, δ is the difference between adjacent grid points, and u_g and v_g are zonal and meridional flow respectively. We also calculate the monthly SLA per grid cell from the mean dynamic topography (MDT) and the surface current magnitude, U:

$$U = \sqrt{u_g^2 + v_g^2}, \tag{13}$$

https://doi.org/10.5194/egusphere-2026-4414
Preprint. Discussion started: 11 August 2026

4. Formal Error Calculation

The formal error is calculated using the standard error of the ocean-lead and mode offsets, alongside the crossover uncertainty method detailed by Giles et al. (2012) and Armitage et al. (2016), and then these are added in quadrature to calculate the total uncertainty of the product.

4.1. Standard Error Calculation

4.1.1. Offset Climatologies

To quantify the SLA uncertainty associated with the ocean-lead (O/L) and CryoSat-2 offsets, we estimate the standard error of the monthly climatological offset. We use the RMS of each offset's monthly climatology as calculated in Sect. 3.2. and Sect. 3.3. respectively to characterise the variability within each month. Using this, RMS_m, and number of valid points per month, N_m, SE is calculated as

$$SE_m = \frac{RMSE_m}{\sqrt{N_m}}, \quad (14)$$

This provides a measure of the climatology precision for each offset as it estimates climatological seasonal variability.

4.1.2. Crossover Locations

Crossover locations are defined as locations where there are along-track measurements within 100 m (Giles et al., 2012) and 10 days of each other (A Hooley, 2018) for each satellite during the overlapping period. We calculate SSH differences south of 60°S, due to the sparsity of CryoSat-2 crossover locations north of this, using

$$\Delta h = Elevation_A - Elevation_B, \quad (15)$$

where $Elevation_A$ and $Elevation_B$ are the adjacent SSH measurements, before binning each Δh pair onto the product grid of 1° longitude by 0.5° latitude. We calculate the monthly RMS of Δh in each grid cell as:

$$RMSE = \sqrt{\frac{\Delta h^2}{N}}, \quad (16)$$

with the N used in the Eq. (16) the number of Δh crossover pairs in that grid cell (from CryoSat-2, Envisat, or both in overlapping bins). We then calculate the mean over time to get a spatial representation of crossover RMS. Using this and the number of satellite passes per month in each grid cell, we calculate the standard error (SE) of the crossover elevation differences

https://doi.org/10.5194/egusphere-2026-4414
Preprint. Discussion started: 11 August 2026

$$Standard\ Error = \frac{RMSE_{\Delta h}}{\sqrt{N}}, \tag{17}$$

with N referring to the number of satellite passes contributing to that grid cell. We produce a hybrid estimate of the SSH uncertainty for the overlapping period for bins where there are inter-satellite crossover locations. To do this we use ΣN and $\Sigma\Delta h^2$ in Eq. (16) before calculating the SE in the overlapping bins in Eq. (17). This pooling assumes that the two satellites provide independent samples of the same underlying elevation field, allowing their variances and sample counts to be combined without bias. Otherwise, in single satellite bins, we calculate the RMSE and SE from either only CryoSat-2 or Envisat.

As with the ocean-lead and CrysoSat-2 offsets, we calculate a monthly climatology of RMS and SE by averaging the per-month hybrid RMS and SE fields at each grid cell over the overlapping period to represent seasonal variability in the final error calculation.

We then apply a 150-km Gaussian spatial filter to the climatological RMS and SE fields to reduce small-scale noise and calculate the area-weighted averages over the grid south of 60˚S to produce Figure 6. The areas of increased uncertainty are where there is shallow complex bathymetry, like in the Indian Sector or near the West Antarctic Peninsula. This complexity increases eddy and tidal activity which is aliased by the along-track observations despite their respective <10-day separation and post-processing correction (Esa, 2019).

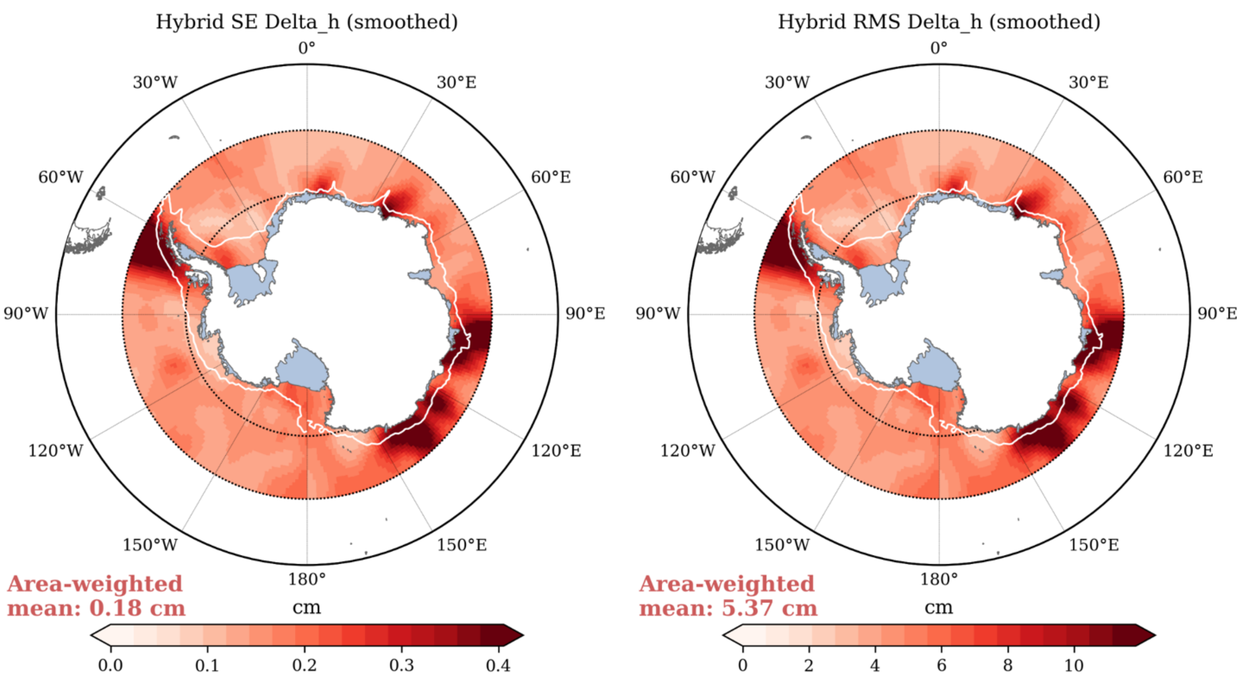

https://doi.org/10.5194/egusphere-2026-4414
Preprint. Discussion started: 11 August 2026

Figure 6: Area weighted SE (left) and RMS (right) of the gridded along-track independent differences at crossover locations for Envisat or CryoSat-2. Due to the distribution of crossover locations, some grid cells contain data from only one satellite whereas others contain crossover data from both satellites. The SE and RMS plots and weighted-means above include all data per grid cell – regardless of satellite source. This results in a 'hybrid' estimation of uncertainty due to atmospheric processes regardless of the measuring satellite.

By calculating the uncertainty in this manner, we combined multiple different sources such as instantaneous DOT variability, geophysical corrections, instrumental noise and orbit error (Armitage et al., 2016). This removes the need to calculate individual component uncertainty – a challenge in Antarctica due to the lack of constraining data – and allows us to provide a total elevation error.

4.2. Geoid Uncertainty

We use the method from Segabinazzi Dotto (2019) to calculate the uncertainty of our product due to geoid variations. Our product is a sea level *anomaly* product so absolute geoid offsets do not affect long-term trends; however, we wanted to quantify the intra-geoid seasonal variability. Therefore, we calculate the standard deviation of the monthly mean SSH difference between geoid models and calculate this uncertainty as 0.12 cm.

4.3. Total Uncertainty

To finalise our uncertainty we add, in quadrature, the climatology for the ocean-lead offsets, mode offsets, and cross-over standard error. We then add the geoid uncertainty of 0.12 cm to produce Figure 7. The overall uncertainty is taken as the mean across all months and is 0.78 cm.

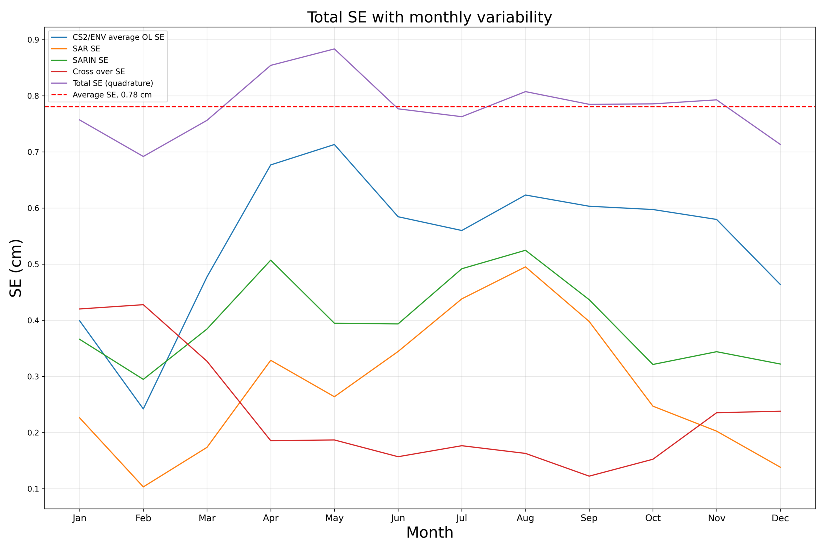

Figure 7: Monthly SE climatologies for each component of uncertainty. The total SE uses addition through quadrature to calculate the overall uncertainty as the purple line, the mean of which is 0.78 cm.

https://doi.org/10.5194/egusphere-2026-4414
Preprint. Discussion started: 11 August 2026

5. Results

5.1 The Final Dataset

The final dataset is a 1˚ longitude by 0.5˚ latitude gridded SLA product which uses the overlap period for Envisat and CryoSat-2 to create continuous 2002-2024 coverage. We find using the EGM2008 geoid and median statistics for the climatology and offset averages result in the root mean squared lowest error at 0.52 cm and the second lowest at 0.53 cm using GOCO05c. Hence, we present those products here. The data fields available in the product are shown in Table A2 for the monthly product. This product is available through (https://doi.org/10.5281/zenodo.21454185).

5.2. Validation

5.2.1. Multi-mission Satellite Data

We first validate our DOT product against the CMEMS absolute dynamic topography (ADT) dataset. We calculate anomalies for both using the temporal mean for the overlapping period between 10-2002 to 12-2024 at each grid cell.
We also use only cells where CMEMS observations are present for >80% of the time series and mask months where < 30 % of grid cells contain valid data. This process manages the impact of low data coverage in sea ice regions without loss of temporal coverage. Pearson correlation coefficients are then calculated independently at each grid cell. Figure 8 shows the correlation map where there is a 95% confidence level ($p<0.05$).

For the EGM2008 product, the area-weighted correlation coefficient is 0.93 and root mean square difference (RMSD) of 0.77 cm which shows strong agreement between the two products.

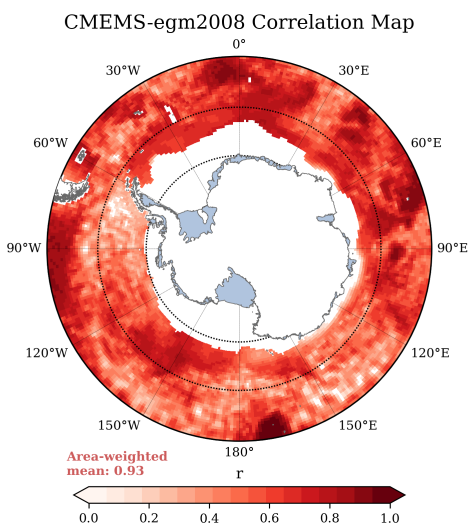

Figure 8: CMEMS-SLA product correlation map for EGM2008 monthly product for months with data more than 80% of the time and where more than 30% of grid cell contain valid data.

https://doi.org/10.5194/egusphere-2026-4414
Preprint. Discussion started: 11 August 2026

In addition to the CMEMS Global L4 product we use the recent multi-mission satellite dataset from Mosneron Dupin et al. (2025) which uses Envisat, CryoSat-2, SARAL/Altika, and Sentinel-3A data between 2003-2021 to validate our product in sea ice regions. The products have independent processing pipelines and the duration of Mosneron Dupin et al. (2025) product increases confidence in the later stages of our product where there is no BPR data. Between 2003-01-01 and 2021-12-01 the total area-weighted average correlation is strong at 0.8 with a root mean square difference (RMSD) of 1.1 cm. We also calculate the correlation North and South of 65˚S to assess where the highest uncertainty occurs. These regions have correlations of 0.96 and 0.47, highlighting the larger uncertainty near the coast as seen in Figure 9.

The decrease in near-coast correlation is possibly due to the inclusion of SARIn CryoSat-2 data in our product compared to the exclusion in the Mosneron Dupin et al. (2025) product. This results in our product having an increased the amount of data on the continental shelf despite their inclusion of the other satellite data does lessen the error in the coastal region. The inter-product acquisition and processing differences outlined in Sect. 2.2.1, explains the much higher correlation found above when we spilt each product with the 65˚S line.

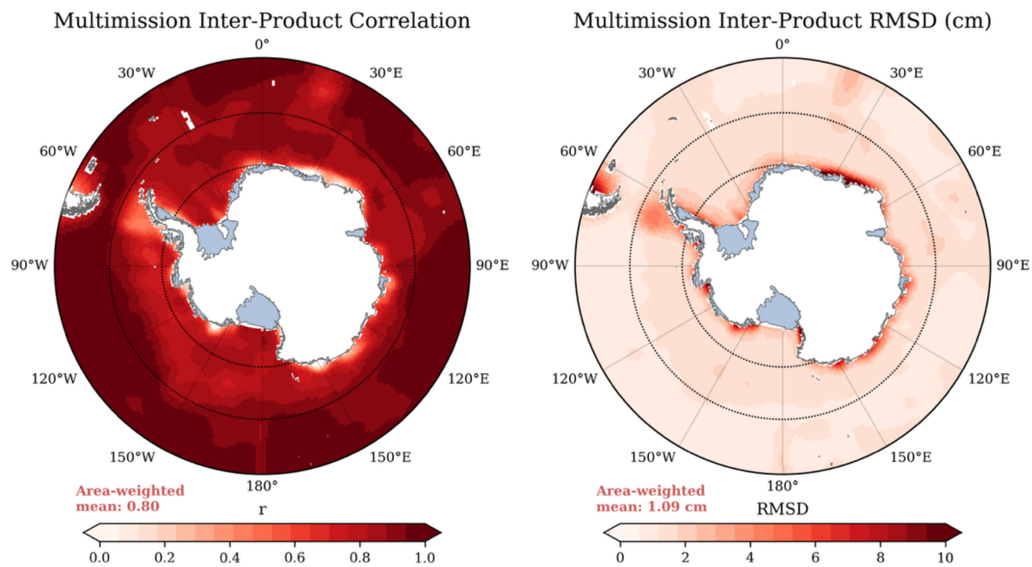

Figure 9: Map of the correlation (left) between our SLA product (using the EMG2008 geoid) and the SLA product from Mosneron Dupin et al. (2025) and residual mean square difference (RMSD) (right).

5.2.2. Bottom Pressure

For both bottom pressure data sets, we calculate the monthly average to match our product's temporal resolution before detrending and calculating a monthly anomaly. For the BPR data we use the residual pressure which is the pressure after the

https://doi.org/10.5194/egusphere-2026-4414
Preprint. Discussion started: 11 August 2026

tidal prediction and drift have been removed. From these we calculate the correlation between the bottom pressure anomaly and the product SLA for each grid cell during the overlapping period. To assess the overall agreement, we average all grid cells with where $p \leq 0.05$ to focus on areas where the relationship is robust. The correlation plots for the BPR stations are shown in Figure 10 with comparable figures for six BPM stations in A1.

For both, the strongest correlation is typically where a recorder or mooring is close to the coast (i.e., on the shelf) and typically circumpolar which suggests all datasets capture the dominant mode of variability there. To quantify the near-shelf correlation we calculate the average correlation across all grid cells south of 60˚S where the correlation is significant, $p \leq 0.05$ and call this the 'spatial correlation'. We then calculate the average SLA for the selected grid cells for each month and compare this to both sets of BPR and BPM time series – the 'temporal correlation'. Table 4 highlights an increase in correlation using the temporal correlation method which shows our product captures temporal variability well.

In the BPR dataset, the lowest correlation occurs at PIES_17_1. This is possibly due to its distal location from the coast (over 550 km away) which results in mesoscale processes dominating the SSH variability rather than the large-scale processes like the Southern Mode (Hughes et al., 1999). This suggestion is supported by (Mosneron Dupin et al., 2025) who have a higher correlation of 0.52 at this BPR when using the daily product smoothed with a 15-day rolling average and spatial resolution of 25 km compared to our product's monthly and 1˚ longitude by 0.5˚ latitude resolution.

Table 4: BPR correlation table with BPR full name and code used in Fig.10. Spatial correlation is the average correlation coefficient between product SSH and the BPR SSH where correlation is significant ($p \leq 0.05$). Temporal correlation is the correlation between the BPR SSH and the average SSH across all selected grid points.

BPR	BPR Code	Spatial Correlation ($p \leq 0.05$)	Average Temporal Correlation ($p \leq 0.05$)
MyrtleB	MyrtleB	0.74	0.94
MyrtleC	MyrtleC	0.55	0.76
Drakes Passage	DRP	0.38	0.60
Drakes Passage (deep)	DRP_deep	0.47	0.74
ANT_17_1	PIES_17_1	0.37	0.58

In the OCEAN:ICE dataset, we generally see similar relationship with circumpolar correlation patterns which supports the use of our product for circumpolar study. We find that when using the nearest point method for correlation, some areas close to the coast show a weaker correlation (Fig. A2) for example in the highly dynamic Thwaites Glacier region located in the Amundsen Sea, West Antarctica. This result is likely due to lower quality SSH data near the coast due to the presence small-scale ocean features such as eddies, SSH signals from complex bathymetry and bay morphology or the impact of icebergs/fast ice. In addition to satellite limitations, we see some variability in BPM data quality (Fig. A3) for both near coast and complex bathymetry, such as the Maud Rise, regions which can also impact the calculated correlation. When instead we calculate the temporal correlation mean, average SLA for all significant ($p \leq 0.05$) cells south of 60˚S, the correlation increases (Fig. 11).

https://doi.org/10.5194/egusphere-2026-4414
Preprint. Discussion started: 11 August 2026

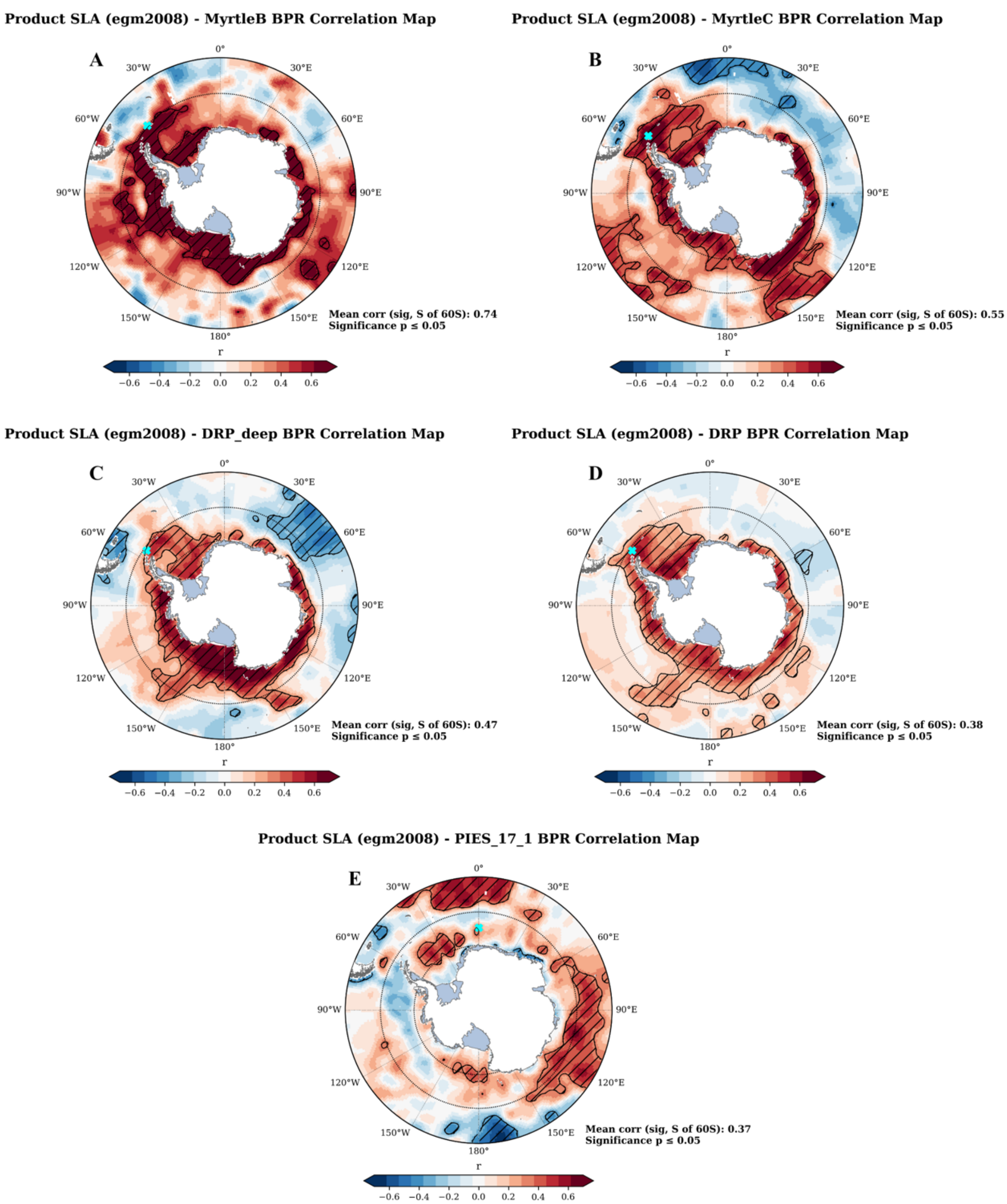

Figure 10: Correlation maps between the SLA product (using the EGM2008 geoid) and de-tided BPR time series for a) MyrtleB, b) MyrtleC, c) DRP, d) DRP_deep, and e) PIES_17_1. We have de-trended both the BPR times series and each grid cell's SLA. BPR locations are marked by the thick cyan crosses. The hatched areas are where the correlation p-value ≤ 0.05. Reported correlations are the area-weighted mean values where correlation is significant (p ≤ 0.05).

https://doi.org/10.5194/egusphere-2026-4414
Preprint. Discussion started: 11 August 2026

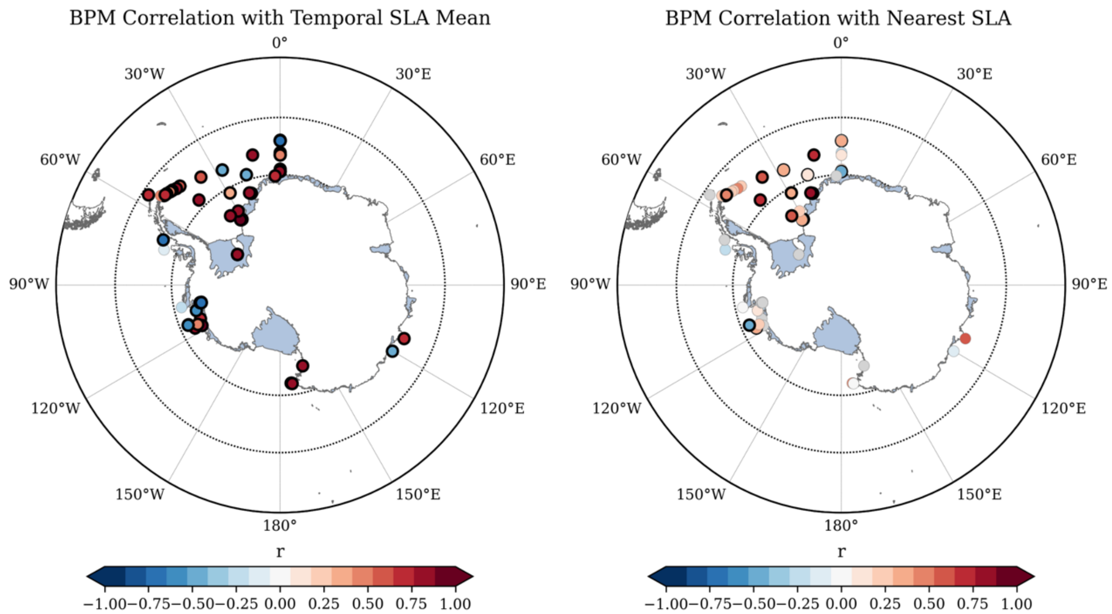

Figure 11: Left: Temporal correlation heat map for all statistically significant, p≤0.05, grid cells south of 60˚S between the between the SLA product (using the EGM2008 geoid) and BPM time series dataset. Right: Correlation heat map between the time series for each BPM ocean bottom pressure anomaly and nearest grid cell SLA. Grey stations are stations which have <10 valid cells per month. In the left-hand plot this relates to too few significantly correlated cells per month and in the right-hand plot reflects either an area of low data quality or ice cover. For both plots the thick black outline marks BPMs where correlation is statistically significant (p≤0.05).

5.2.3. Southern Annular Mode

Similarly to the BPR, we expect our product to capture the seasonal to annual variation of SLA due to atmospheric forcing from the Southern Annular Mode (SAM) index. This index the zonal pressure difference between latitudes 40˚S and 65˚S which leads to intensification of westerly winds between 50-70˚S when positive and westerly weakening when negative (Marshall, 2003). As westerlies drive Ekman pumping this in turn leads to increased northward transport when positive and, therefore, a decrease in coastal SSH. The opposite occurs when the SAM index decreases and the result is negative circumpolar correlation between SSH and the SAM index. We clearly see a negative relationship at the coast and 'see-saw' effect in the open ocean in Figure 12 which further validates our product.

https://doi.org/10.5194/egusphere-2026-4414
Preprint. Discussion started: 11 August 2026

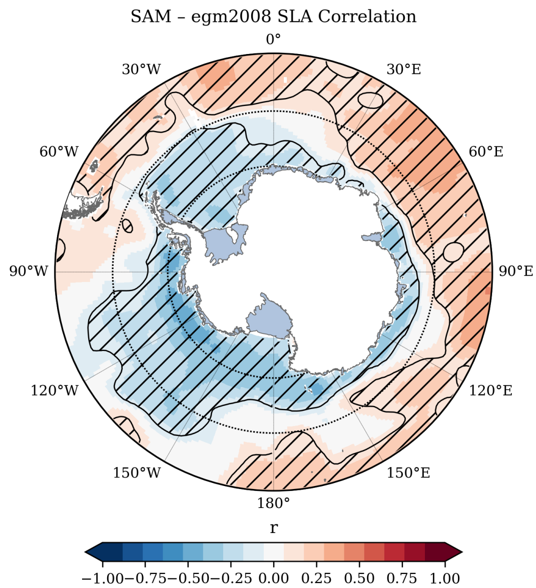

480 **Figure 12: Correlation map between the SLA product (using the EGM2008 geoid) and the SAM index. The hatched areas are where the correlation p-value ≤ 0.05.**

6. Conclusions

We have presented a 1˚ longitude by 0.5˚ latitude gridded circumpolar SLA product south of 50˚S which is continuous across the transition from the open ocean to the seasonally sea ice covered regions and is over 20 years long spanning 2002-2024. We have used the standard altimetry processing method outlined by Peacock and Laxon (2004) which separates ocean and lead reflectors and calculates the offset between them to correct for sea ice cover. Using a similar approach, the offset between the different acquisition modes (LRM, SAR, and SARIn) of CryoSat-2 were calculated and corrected for. From the independent satellite timeseries, we calculate the SSH offset during the overlapping period 01/11/2010 to 01/03/2012, 4.3 cm for the EGM2008 geoid, and level CryoSat-2 data to Envisat data to produce a combined dataset.

Although this dataset uses a pre-established method for the combination of two satellite's data it is unique due to its duration and spatial resolution and is, to date, the longest product covering both the open ocean and coastal Antarctic region. In the Southern Ocean previous work typically has study periods of 4-6 years (Auger et al., 2022; Dotto et al., 2018; Naveira Garabato et al., 2019). At 22 years, this dataset increases temporal duration by over a decade for many studies and thus broadens our ability to study long-term processes as well as the relationships between processes of different timescales.

An exception to this temporal increase is the work of Mosneron Dupin et al. (2025) where the authors present a 19-year product. A key difference here is our inclusion of the highest resolution CryoSat-2 mode, SARIn, and so sea surface height

https://doi.org/10.5194/egusphere-2026-4414
Preprint. Discussion started: 11 August 2026

measurements at the ice sheet margins (Wingham et al., 2006). Additionally Mosneron Dupin et al. (2025) use a uniform 75 km x 75 km grid throughout the product domain whereas we use a geographical coordinate system which results an absolute decrease in grid size closer to the poles. These two differences increase on-shelf resolution and subsequently will be suitable for ocean-ice dynamics provided their length scale is large enough as mesoscale variability is beyond the scope of this product.

We also calculate the formal error using the standard error of the monthly climatologies for the ocean-lead offsets, mode offsets and cross-over location SSH differences which we add in quadrature. In addition to this, we consider the intra-seasonal uncertainty due to geoid selection using the standard deviation of SSH difference climatologies between four geoid (EGM2008, GOCO05, EIGEN6S4V2 and GOCO2025s) and add this, 0.12 cm, to the final error. The final product uncertainty is 0.78 cm is comparable to monthly SSH uncertainties reported in similar studies: 1.1 cm for the Arctic Armitage et al. (2016), 0.56 cm and 0.81 cm for the open ocean and ice-covered ocean A Hooley (2018), and 1.3 cm from Mosneron Dupin et al. (2025).

Further to this uncertainty calculation, we validate our product using a range of measurements including SLA CMEMS reconstruction, in situ BPRs, and the multi-mission satellite dataset from Mosneron Dupin et al. (2025). We also use the SAM index to confirm that our product behaves consistently with atmospheric forcing expectations as this has been shown to dominate Southern Ocean SSH variability (Naveira Garabato et al., 2019). Generally, these show a strong correlation with our product with the BPRs and SAM correlation maps exhibiting coastal coherence, which confirms the product's ability to capture on-shelf SSH variation. There are three exceptions to the strong correlation in the PIES_17_1 BPR and 2 BPM stations discussed above. These are in regions of high mesoscale activity or complex topography, both of which result in small scale SSH fluctuations which are hard to capture with the monthly resolution of our product. This again highlights the need for continued study in the Southern Ocean, especially the sea ice zone, where the environment makes both remote and in-situ observations challenging.

For the CMEMS and multi-mission products, we show area-weighted correlations of 0.93 and 0.76 cm respectively across the entire product area. To assess the systematic errors or uncertainties in the ice-covered and coastal regions due to inclusion (our product) and exclusion (product from Mosneron Dupin et al. (2025) of SARIn data, we split the map at 65˚S and mask the few coastal areas which have a high RMSD/low correlation for the multi-mission product. We find the agreement between the two multi-mission products increases from 0.47 to 0.96 in the Southern sector.

This dataset furthers our ability to monitor and investigate long-term processes in the Southern Ocean and the vulnerability of the poorly sampled and studied ice-covered region. For example, at over two decades, shifting atmospheric patterns and subsequent oceanic impacts can be captured and used to deepen the understanding of current system changes and subsequently their impact on other variables, such as sea ice extent surrounding the 2016 decline in Antarctic sea ice. This product provides valuable opportunity to extend work surrounding gyre variability (Dotto et al., 2018), ocean heat content from steric height

https://doi.org/10.5194/egusphere-2026-4414
Preprint. Discussion started: 11 August 2026

calculation (Cocks et al., 2025), or interannual variability in Antarctic Bottom Water export (Auger et al., 2025). Further to this, the pipeline has been designed to support this inclusion of further CryoSat-2 data without processing redesign – again this will increase our ability to work with recent implications of climate forcing and, therefore, highlight areas which are most susceptible to the highly dynamic climate we live in.

Appendix A:

Table A1: Description of file attributes for Envisat and CryoSat-2 files after initial filtering.

Field Description	**Field Name ENVISAT**	**Field Name CyroSat-2**
1 = Ocean, 2 = Lead	SurfaceType	SurfaceType
Days since 1950-01-01	Time	Time
-	Latitude	Latitude
-	Longitude	Longitude
SSH - MSS has not been removed	Elevation	Elevation
Mean Sea Surface Height	MeanSSH	MeanSSH
Number associated with every track	track_num	track_num
1 = Ascending, -1 = Descending	track_dir	track_dir
Percentage ice concentration	ice_conc	ice_conc
1 = Open water, 2 = First year ice, 3 = Multi-year ice, 4 = Ambiguous	sea_ice_type	sea_ice_type
Confidence in sea ice type; 4 = Good, 5 = Excellent	conf_sit	conf_sit
Distance on the WGS84 ellipsoid to the nearest coastline point (m)	distance_m	distance_m
Number of valid points after filtering	N/A	nrows
'LRM', 'SAR', 'SARIN'	N/A	mode
1 = LRM, 2 = SAR, 3 = SARIN	N/A	Retracker
Direction of the previous track	N/A	track_dir_prev
Cumulative sum of direction changes	N/A	row_idx

https://doi.org/10.5194/egusphere-2026-4414
Preprint. Discussion started: 11 August 2026

Table A2: Final product data fields.

Variable Name	Description
dot	Dynamic Ocean Topography
ug	Eastwards geostrophic velocity
vg	Northwards geostrophic velocity
U	Surface current magnitude
land_mask	1 = land, 0 = ocean
intersat_offset	Area-weighted average of the median of binned SLA_env-SLA_cs2 in the overlap period referenced to Envisat's MDT
sla	Sea Level Anomaly

https://doi.org/10.5194/egusphere-2026-4414
Preprint. Discussion started: 11 August 2026

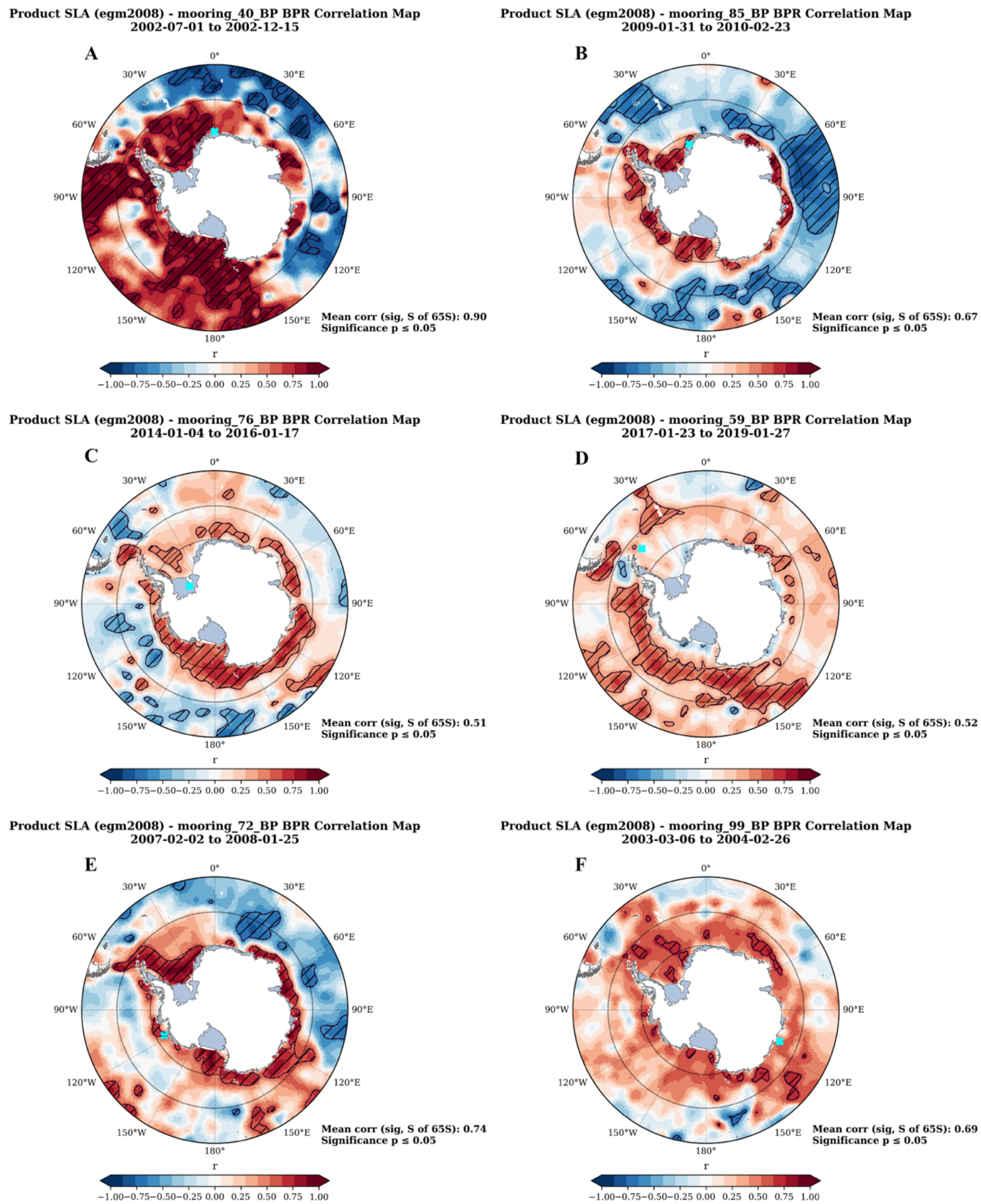

Figure A1: Correlation maps between the SLA product (using the EGM2008 geoid) and BPM time series for stations 40 (A), 85 (B), 76 (C), 59 (D), 72 (E) and 99 (F) which are examples of strong correlation along the Antarctic coastline. BPR locations are marked by the thick cyan crosses. The hatched areas are where the correlation p-value ≤ 0.05.

https://doi.org/10.5194/egusphere-2026-4414
Preprint. Discussion started: 11 August 2026

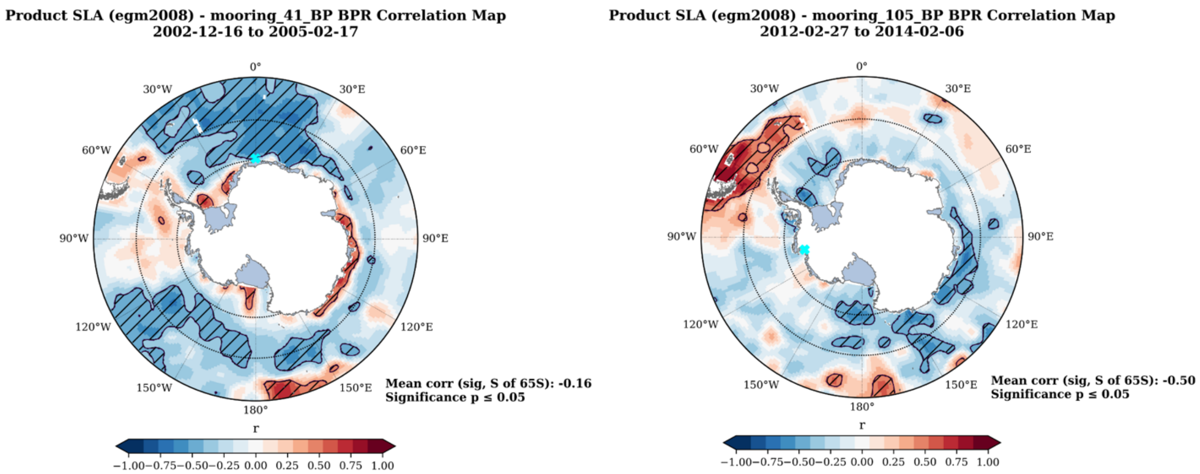

Figure A2: Correlation maps between the SLA product (using the EGM2008 geoid) and BPM time series for stations 41 (left) and 115 (right). BPR locations are marked by the thick cyan crosses. The hatched areas are where the correlation p-value ≤ 0.05. Both are near the coast where mesoscale processes may dominate large-scale processes, despite their locations within the geostrophic contours described by (Marshall, 1995). For station 105 this relationship could be due to high iceberg presence in the Thwaites Glacier region which impacts both the quality of the satellite SSH and the BPM.

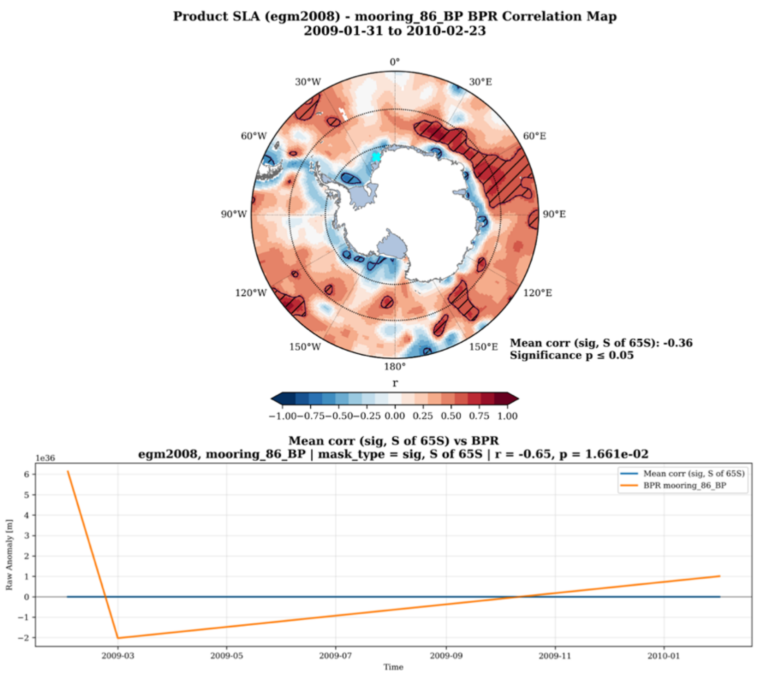

Figure A3: Example of poor BPM data quality at station 86. Top: Correlation maps between the SLA product (using the EGM2008 geoid) and BPM time series for station 86. Bottom: Time series for bottom pressure mooring and 'temporal' (mean SLA values for significant cells south of 60°S) anomalies. BPR location is marked by the thick cyan cross. The hatched areas are where the correlation p-value ≤ 0.05.

https://doi.org/10.5194/egusphere-2026-4414
Preprint. Discussion started: 11 August 2026

Code, data, or code and data availability

Sea level anomaly (SLA) product with geostrophic currents, surface current magnitude, and dynamic ocean topography included for the subpolar Southern Ocean between 50˚S-90˚S and 2002 to 2024. This product uses satellite altimetry from Envisat and CryoSat-2 missions with inter- and intra- satellite offsets corrected for to product a continuous dataset. Ocean and lead reflectors are separated to support sea surface height calculation in the sea ice region. The altimetry product discussed in this article is publicly available from https://doi.org/10.5281/zenodo.21454185.

Supplement link

The link to the supplement will be included by Copernicus, if applicable.

Author contributions

IW, OCD, and AS designed the study. OCD developed the initial product, IW build on this to extend the dataset and include formal error analysis, and AS and ACNG supervised the research. IW prepared the manuscript with all co-authors reviewing and revising the final manuscript.

Competing interests

The authors declare that they have no conflict of interest.

Disclaimer

Copernicus Publications adds a standard disclaimer: "Copernicus Publications remains neutral with regard to jurisdictional claims made in the text, published maps, institutional affiliations, or any other geographical representation in this paper. While Copernicus Publications makes every effort to include appropriate place names, the final responsibility lies with the authors. Views expressed in the text are those of the authors and do not necessarily reflect the views of the publisher."
Please feel free to add disclaimer text at your choice, if applicable.

Acknowledgements

The work presented in this manuscript was made possible due to data processing by CPOM and the University of Leeds, particularly Andy Ridout and Anna Hogg, Oana Dragomir's PhD work combining the two satellites until 2018 and her feedback throughout the development of this product, the OCEAN:ICE dataset shared by Pierre Dutrieux and Cosme Monseron-Dupin and feedback from all coauthors throughout its development. During product development the tool Claude

AI was used by Isabelle White for code debugging and streamlining. This work has been supported by the European Space Agency (ESA) as part of the ESA CLIMATE-SPACE Tipping Elements Activity via the Tipping Point of the Southern Ocean Overturning (TIPSOO) project https://climate.esa.int/ (last access: 7 November 2025) (ESA contract no. 4000146528/24/I-LR). Alessandro Silvano received funding from NERC (grant no. NE/V014285/1)

Review statement

The review statement will be added by Copernicus Publications listing the handling editor as well as all contributing referees according to their status anonymous or identified.

References

A Hooley, J. M.: Polar Southern Ocean dynamics from satellite altimetry, 2018.

Andersen, O. B., Nielsen, K., Williams, S. D. P., Khan, S. A., and Kern, M.: Artic water level and tides from GNSS-R and satellite altimetry - the Greenland case, AGU Fall Meeting Abstracts, December 01, 20192019.

Armitage, T. W. K., Kwok, R., Thompson, A. F., and Cunningham, G.: Dynamic Topography and Sea Level Anomalies of the Southern Ocean: Variability and Teleconnections, Journal of Geophysical Research: Oceans, 123, 613-630, 10.1002/2017JC013534, 2018.

Armitage, T. W. K., Bacon, S., Ridout, A. L., Thomas, S. F., Aksenov, Y., and Wingham, D. J.: Arctic sea surface height variability and change from satellite radar altimetry and GRACE, 2003–2014, Journal of Geophysical Research: Oceans, 121, 4303-4322, 10.1002/2015JC011579, 2016.

Aublanc, J., Thibaut, P., Guillot, A., Boy, F., and Picot, N.: Ice Sheet Topography from a New CryoSat-2 SARIn Processing Chain, and Assessment by Comparison to ICESat-2 over Antarctica, Remote Sensing, 13, 4508, 2021.

Auger, M., Prandi, P., and Sallée, J.-B.: Southern ocean sea level anomaly in the sea ice-covered sector from multimission satellite observations, Sci Data, 9, 70, 10.1038/s41597-022-01166-z, 2022.

Auger, M., Sallée, J.-B., Thompson, A. F., Pauthenet, E., and Prandi, P.: Southern Ocean Ice-Covered Eddy Properties From Satellite Altimetry, Journal of Geophysical Research: Oceans, 128, e2022JC019363, https://doi.org/10.1029/2022JC019363, 2023.

Auger, M., Spence, P., Morrison, A. K., Naveira Garabato, A., and Silvano, A.: The variability of Antarctic dense water overflows can be observed from space, Commun Earth Environ, 6, 286, 10.1038/s43247-025-02210-7, 2025.

Benveniste, J., Milagro-Perez, M. P., Roca, M., and Levrini, G.: The ENVISAT Radar Altimeter System, Satellite Altimetry for Geodesy, Geophysics and Oceanography, Berlin, Heidelberg, 2004//, 251-259,

Bindschadler, R.: Landsat coverage of the earth at high latitudes, Photogrammetric Engineering and Remote Sensing, 69, 1333-1339, 10.14358/pers.69.12.1333, 2003.

Bouffard, J., Naeije, M., Banks, C. J., Calafat, F. M., Cipollini, P., Snaith, H. M., Webb, E., Hall, A., Mannan, R., Féménias, P., and Parrinello, T.: CryoSat ocean product quality status and future evolution, Advances in Space Research, 62, 1549-1563, https://doi.org/10.1016/j.asr.2017.11.043, 2018.

Chelton, D. B., Ries, J. C., Haines, B. J., Fu, L.-L., and Callahan, P. S.: Chapter 1 Satellite Altimetry, in: International Geophysics, edited by: Fu, L.-L., and Cazenave, A., Academic Press, 1-ii, https://doi.org/10.1016/S0074-6142(01)80146-7, 2001.

Chuter, S. J. and Bamber, J. L.: Antarctic ice shelf thickness from CryoSat-2 radar altimetry, Geophysical Research Letters, 42, 10,721-710,729, https://doi.org/10.1002/2015GL066515, 2015.

CMEMS: Global Ocean Gridded L 4 Sea Surface Heights And Derived Variables Reprocessed 1993 Ongoing, https://doi.org/10.48670/moi-00148, 2024.

Cocks, J., Silvano, A., Naveira Garabato, A. C., Dragomir, O., Schifano, N., Hogg, A. E., and Marzocchi, A.: Satellite-derived steric height in the Southern Ocean: trends, variability, and climate drivers, Ocean Sci., 21, 1609-1625, 10.5194/os-21-1609-2025, 2025.
Doddridge, E. W., Hobbs, W. R., Auger, M., Boyd, P. W., Chua, S. M. T., Cook, S., Corney, S., Emmerson, L., Fraser, A. D., Heil, P., Kelly, N., Lannuzel, D., Li, X., Liniger, G., Massom, R. A., Meyer, A., Reid, P., Southwell, C., Spence, P., Steketee, A., Swadling, K. M., Teder, N., Wienecke, B., Wongpan, P., and Yamazaki, K.: Impacts of Antarctic summer sea-ice extremes, PNAS Nexus, 4, 10.1093/pnasnexus/pgaf164, 2025.
Dotto, T. S., Naveira Garabato, A., Bacon, S., Tsamados, M., Holland, P. R., Hooley, J., Frajka-Williams, E., Ridout, A., and Meredith, M. P.: Variability of the Ross Gyre, Southern Ocean: Drivers and Responses Revealed by Satellite Altimetry, Geophysical Research Letters, 45, 6195-6204, https://doi.org/10.1029/2018GL078607, 2018.
Downes, S. M., Budnick, A. S., Sarmiento, J. L., and Farneti, R.: Impacts of wind stress on the Antarctic Circumpolar Current fronts and associated subduction, Geophysical Research Letters, 38, https://doi.org/10.1029/2011GL047668, 2011.
Dragomir, O. C.: Dynamics of the subpolar southern ocean response to climate change, 2024.
ESA: CryoSat-2 Product Handbook, 2019.
Fecher, T., Pail, R., Gruber, T.: The combined gravity field model GOCO05c, EGU, Vienna, 20162016.
Förste, C. B., Sean; Abrykosov, Oleh; Rudenko, Sergiy; Lemoine, Jean-Michel; Marty, Jean-Charles; Neumayer, Karl Hans; Biancale, Richard: EIGEN-6S4 A time-variable satellite-only gravity field model to d/o 300 based on LAGEOS, GRACE and GOCE data from the collaboration of GFZ Potsdam and GRGS Toulouse. V. 2.0. , GFZ Data Services, 2016.
Gallaher, D. and Campbell, G. G.: Nimbus High Resolution Infrared Radiometer Digital Swath Data L1, HDF5, Version 1, NASA National Snow and Ice Data Center Distributed Active Archive Center [dataset], 10.5067/NIMBUS/NMHRIR1H, 2013.
Giles, K. A., Laxon, S. W., Ridout, A. L., Wingham, D. J., and Bacon, S.: Western Arctic Ocean freshwater storage increased by wind-driven spin-up of the Beaufort Gyre, Nature Geoscience, 5, 194-197, 10.1038/ngeo1379, 2012.
Gong, D. and Wang, S.: Definition of Antarctic Oscillation index, Geophysical Research Letters, 26, 459-462, https://doi.org/10.1029/1999GL900003, 1999.
Gourmelen, N., Escorihuela, M. J., Shepherd, A., Foresta, L., Muir, A., Garcia-Mondéjar, A., Roca, M., Baker, S. G., and Drinkwater, M. R.: CryoSat-2 swath interferometric altimetry for mapping ice elevation and elevation change, Advances in Space Research, 62, 1226-1242, https://doi.org/10.1016/j.asr.2017.11.014, 2018.
Gülk, B., de Lavergne, C., Sallée, J.-B., Madec, G., Rousset, C., Abelló, A. O., and Coulon, V.: The Response of the Global Overturning Circulation to Recent and Projected Antarctic Meltwater Changes, Journal of Geophysical Research: Oceans, 131, e2026JC024622, https://doi.org/10.1029/2026JC024622, 2026.
Inserra, G., Buono, A., Nunziata, F., Migliaccio, M., Parmiggiani, F., and Aulicino, G.: Characterization of the Terra Nova Bay Polynya Using Dual-Polarimetric C-Band SAR Measurements, IEEE Journal of Oceanic Engineering, 49, 856-869, 10.1109/JOE.2024.3356569, 2024.
Jonathan, B. and Charles r, B.: A comparison of satellite-altimetry and ice-thickness measurements of the Ross Ice Shelf, Antarctica, Annals of Glaciology, 20, 357-364, 10.3189/1994AoG20-1-357-364, 1994.
Lacroix, P., Legrésy, B., Coleman, R., Dechambre, M., and Rémy, F.: Dual-frequency altimeter signal from Envisat on the Amery ice-shelf, Remote Sensing of Environment, 109, 285-294, https://doi.org/10.1016/j.rse.2007.01.007, 2007.
Leberl, F., Raggam, J., Elachi, C., and Campbell, W. J.: Sea ice motion measurements from SEASAT SAR images, Journal of Geophysical Research: Oceans, 88, 1915-1928, https://doi.org/10.1029/JC088iC03p01915, 1983.
Lelièvre, Y., Lawnizack, G., Ayoub, N. K., d'Ovidio, F., du Châtelet, É. A., Zampolli, M., Haralabus, G., Courcot, L., Collin, P.-Y., and Saucède, T.: Coastal hydrodynamics at the sub-Antarctic Possession Island (Crozet archipelago) inferred from bedform structures and sediment properties, Marine Geology, 485, 107559, https://doi.org/10.1016/j.margeo.2025.107559, 2025.
Li, X., Cai, W., Meehl, G. A., Chen, D., Yuan, X., Raphael, M., Holland, D. M., Ding, Q., Fogt, R. L., Markle, B. R., Wang, G., Bromwich, D. H., Turner, J., Xie, S.-P., Steig, E. J., Gille, S. T., Xiao, C., Wu, B., Lazzara, M. A., Chen, X., Stammerjohn, S., Holland, P. R., Holland, M. M., Cheng, X., Price, S. F., Wang, Z., Bitz, C. M., Shi, J., Gerber, E. P., Liang, X., Goosse, H., Yoo, C., Ding, M., Geng, L., Xin, M., Li, C., Dou, T., Liu, C., Sun, W., Wang, X., and Song, C.: Tropical teleconnection impacts on Antarctic climate changes, Nature Reviews Earth & Environment, 2, 680-698, 10.1038/s43017-021-00204-5, 2021.

https://doi.org/10.5194/egusphere-2026-4414
Preprint. Discussion started: 11 August 2026

Liang, W., Li, J., Xu, X., Zhang, S., and Zhao, Y.: A High-Resolution Earth's Gravity Field Model SGG-UGM-2 from GOCE, GRACE, Satellite Altimetry, and EGM2008, Engineering, 6, 860-878, https://doi.org/10.1016/j.eng.2020.05.008, 2020.

Maraldi, C., Lyard, F., Testut, L., and Coleman, R.: Energetics of internal tides around the Kerguelen Plateau from modeling and altimetry, Journal of Geophysical Research: Oceans, 116, https://doi.org/10.1029/2010JC006515, 2011.

Marshall, D.: Topographic Steering of the Antarctic Circumpolar Current, Journal of Physical Oceanography, 25, 1636-1650, https://doi.org/10.1175/1520-0485(1995)025<1636:TSOTAC>2.0.CO;2, 1995.

Marshall, G. J.: Trends in the Southern Annular Mode from Observations and Reanalyses, Journal of Climate, 16, 4134-4143, https://doi.org/10.1175/1520-0442(2003)016<4134:TITSAM>2.0.CO;2, 2003.

McCandles, S. W.: The origin, evolution and legacy of SEASAT, 32-34 vol.31 pp., 10.1109/IGARSS.2003.1293669, 2003.

Mercier, A., Myllymäki, M., Hovi, A., Schraik, D., and Rautiainen, M.: Exploring the potential of SAR and terrestrial and airborne LiDAR in predicting forest floor spectral properties in temperate and boreal forests, Remote Sensing of Environment, 316, 114486, https://doi.org/10.1016/j.rse.2024.114486, 2025.

Moorman, R.: Response of Antarctic ocean circulation to increased meltwater, 10.25911/5de4da691ed03, 2019.

Mosneron Dupin , C., Sallée, J.-b., and de Lavergne, C.: Reconstructing Sea Level Anomalies in the open and ice-covered Southern Ocean from 2003 to 2021, 10.5194/essd-2025-653, 2025.

Mosneron Dupin, C., Sallée, J. B., and de Lavergne, C.: Reconstructing Sea Level Anomalies in the open and ice-covered Southern Ocean from 2003 to 2021, Earth Syst. Sci. Data Discuss., 2025, 1-29, 10.5194/essd-2025-653, 2025.

Naveira Garabato, A. C., Dotto, T. S., Hooley, J., Bacon, S., Tsamados, M., Ridout, A., Frajka-Williams, E. E., Herraiz-Borreguero, L., Holland, P. R., Heorton, H. D. B. S., and Meredith, M. P.: Phased Response of the Subpolar Southern Ocean to Changes in Circumpolar Winds, Geophysical Research Letters, 46, 6024-6033, https://doi.org/10.1029/2019GL082850, 2019.

Öhlinger, F., Mayer-Gürr, T., Krauß, S., Dumitraschkewitz, P., Süsser-Rechberger, B., Strasser, A., Tieber-Hubmann, C., & Brockmann, J. M. : The satellite-only gravity field model GOCO2025s [Data set]. [dataset], 2025.

Pan, B., Yuan, X., Li, T., Lai, T., Wang, X., Xu, C., and Huang, H.: First Retrieval of Sea Surface Currents Using L-Band SAR in Satellite Formation, 10.3390/rs17010131, 2025.

Peacock, N. R. and Laxon, S. W.: Sea surface height determination in the Arctic Ocean from ERS altimetry, Journal of Geophysical Research: Oceans, 109, https://doi.org/10.1029/2001JC001026, 2004.

Prandi, P., Ablain, M., Cazenave, A., and Picot, N.: A New Estimation of Mean Sea Level in the Arctic Ocean from Satellite Altimetry, Marine Geodesy, 35, 61-81, 10.1080/01490419.2012.718222, 2012.

Resti, A., Benveniste, J., Roca, M., Levrini, G., and Johannessen, J. A.: THE ENVISAT RADAR ALTIMETER SYSTEM (RA-2),

Roca, M., Laxon, S., and Zelli, C.: The EnviSat RA-2 Instrument Design and Tracking Performance, IEEE Transactions on Geoscience and Remote Sensing, 47, 3489-3506, 10.1109/TGRS.2009.2020793, 2009.

Rucci, A., Ferretti, A., Monti Guarnieri, A., and Rocca, F.: Sentinel 1 SAR interferometry applications: The outlook for sub millimeter measurements, Remote Sensing of Environment, 120, 156-163, https://doi.org/10.1016/j.rse.2011.09.030, 2012.

Rye, C. D., Naveira Garabato, A. C., Holland, P. R., Meredith, M. P., George Nurser, A. J., Hughes, C. W., Coward, A. C., and Webb, D. J.: Rapid sea-level rise along the Antarctic margins in response to increased glacial discharge, Nature Geoscience, 7, 732-735, 10.1038/ngeo2230, 2014.

Schmid, P. E., Goddard Space Flight, C., and United, S.: Atmospheric tracking errors at S- and C- band frequencies, NASA TN D-3470, iii, 33 p., National Aeronautics and Space Administration, Washington, D.C. : [For sale by the Clearinghouse for Federal Scientific and Technical, Springfield, Virginia 20230], iii, 33 p. pp.1966.

Segabinazzi Dotto, T.: Dynamics of the Southern Ocean Circulation Off West Antarctica., University of Southampton, 184pp, 2019.

Stewart, R. H.: Seasat: Results of the Mission, Bulletin of the American Meteorological Society, 69, 1441-1447, https://doi.org/10.1175/1520-0477(1988)069<1441:SROTM>2.0.CO;2, 1988.

Teleti, P. R. and Luis, A. J.: Sea Ice Observations in Polar Regions: Evolution of Technologies in Remote Sensing, International Journal of Geosciences, Vol.04No.07, 20, 10.4236/ijg.2013.47097, 2013.

Thresher, R. E., Rintoul, S. R., Fallon, S. J., Richer de Forges, S., Neil, H., Trotter, J. A., Proctor, C., and Tracey, D. M.: Millennial-scale Atlantic overturning circulation led by the Southern Ocean, Nature Geoscience, 19, 520-525, 10.1038/s41561-026-01959-6, 2026.

https://doi.org/10.5194/egusphere-2026-4414
Preprint. Discussion started: 11 August 2026

Tilling, R., Ridout, A., and Shepherd, A.: Assessing the Impact of Lead and Floe Sampling on Arctic Sea Ice Thickness Estimates from Envisat and CryoSat-2, Journal of Geophysical Research: Oceans, 124, 7473-7485, https://doi.org/10.1029/2019JC015232, 2019.

van Wijk, E. M. and Rintoul, S. R.: Freshening drives contraction of Antarctic Bottom Water in the Australian Antarctic Basin, Geophysical Research Letters, 41, 1657-1664, https://doi.org/10.1002/2013GL058921, 2014.

Veillard, P., Prandi, P., Pujol, M.-I., Daguzé, J.-A., Piras, F., Dibarboure, G., and Faugère, Y.: Arctic and Southern Ocean polar sea level maps and along-tracks from multi-mission satellite altimetry from 2011 to 2021, Frontiers in Marine Science, Volume 11 - 2024, 10.3389/fmars.2024.1419132, 2024.

Wang, F., Bamber, J., and Cheng, X.: Accuracy and Performance of CryoSat-2 SARIn Mode Data Over Antarctica, Geoscience and Remote Sensing Letters, IEEE, PP, 1-5, 10.1109/LGRS.2015.2411434, 2015.

Wernecke, A. and Kaleschke, L.: Lead detection in Arctic sea ice from CryoSat-2: quality assessment, lead area fraction and width distribution, The Cryosphere, 9, 1955-1968, 10.5194/tc-9-1955-2015, 2015.

Wingham, D. J., Francis, C. R., Baker, S., Bouzinac, C., Brockley, D., Cullen, R., de Chateau-Thierry, P., Laxon, S. W., Mallow, U., Mavrocordatos, C., Phalippou, L., Ratier, G., Rey, L., Rostan, F., Viau, P., and Wallis, D. W.: CryoSat: A mission to determine the fluctuations in Earth's land and marine ice fields, Advances in Space Research, 37, 841-871, https://doi.org/10.1016/j.asr.2005.07.027, 2006.

Wyatt, J. K., Bindoff, N. L., Foppert, A., Phillips, H. E., and Rintoul, S. R.: Observed Trends and Variability in the Water Masses of the Southern Ocean, Journal of Geophysical Research: Oceans, 131, e2025JC023852, https://doi.org/10.1029/2025JC023852, 2026.

Zhang, B., Wang, Z., An, J., Liu, T., and Geng, H.: A 30-year monthly 5 km gridded surface elevation time series for the Greenland Ice Sheet from multiple satellite radar altimeters, Earth Syst. Sci. Data, 14, 973-989, 10.5194/essd-14-973-2022, 2022.

Zhou, S., Dutrieux, P., Mosneron-Dupin, C., and Hattermann, T.: OCEAN ICE pan-Antarctic near bottom pressure record, SEANOE [dataset], 10.17882/109453, 2025.

Zwally, J. a. A. B. S. a. G. A. f. t. A. a. G. I., Sheets, V. B., Colorado USA. NASA National Snow and Ice, and https://doi.org/10.5067/MTIF60G86H86., D. C. D. A. A. C.: Seasat and GEOSAT Altimetry for the Antarctic and Greenland Ice Sheets, NASA National Snow and Ice
Data Center Distributed Active Archive Center, 1997.